

## Higher-order skin effect and its observation in an acoustic kagome lattice

Jia-Xin Zhong<sup>1,\*</sup> Pedro Fittipaldi de Castro<sup>2,\*</sup> Tianhong Lu<sup>1,2</sup> Jeewoo Kim,<sup>1</sup> Mourad Oudich,<sup>1,3</sup> Jun Ji,<sup>1</sup> Li Shi<sup>1,4</sup>, Kai Chen,<sup>4</sup> Jing Lu<sup>1,4,†</sup> Yun Jing<sup>1,‡</sup> and Wladimir A. Benalcazar<sup>1,§</sup>

<sup>1</sup>*Graduate Program in Acoustics, The Pennsylvania State University, University Park, Pennsylvania 16802, USA*

<sup>2</sup>*Department of Physics, Emory University, Atlanta, Georgia 30322, USA*

<sup>3</sup>*Université de Lorraine, CNRS, Institut Jean Lamour, F-54000 Nancy, France*

<sup>4</sup>*Key Laboratory of Modern Acoustics and Institute of Acoustics, Nanjing University, Nanjing 210093, China*

(Received 29 August 2024; revised 7 January 2025; accepted 9 January 2025; published 23 January 2025)

The non-Hermitian skin effect (NHSE) is a distinctive topological phenomenon observed in non-Hermitian systems. Recently, there has been considerable interest in exploring higher-order NHSE occurrences in two and three dimensions. In such systems, topological edge states collapse into a corner while bulk states remain delocalized. Through a Hermitian–non-Hermitian correspondence, this study predicts and experimentally observes the higher-order NHSE in an acoustic kagome lattice possessing nonreciprocal hoppings. By rotating the frequency spectrum and employing complex-frequency excitation techniques, we observe the localization of acoustic energy towards a corner of the lattice in the topologically nontrivial phase, even when the source is located far from that corner. In contrast, the acoustic energy spreads out when excited at the frequencies hosting the bulk states. These observations are unequivocal evidence of the higher-order NHSE.

DOI: 10.1103/PhysRevB.111.014314

### I. INTRODUCTION

Along with quantized bulk signatures, topological boundary states are a hallmark of topological phases of matter. The bulk and boundary properties in these phases are related by a *bulk-boundary correspondence*, initially identified in Hermitian systems and later extended to non-Hermitian systems that exhibit phenomena such as the non-Hermitian skin effect (NHSE) [1–5]. In Hermitian systems, topological boundary states are characterized by topological invariants of the bulk states within the system. A  $d$ -dimensional system with  $L^d$  degrees of freedom in an  $n$ th-order topological phase has  $O(L^{d-n})$  boundary states [6–8]. Recent studies have generalized the NHSE in one dimension to the high-order NHSE in higher dimensions [6,9–13], showing that systems with an  $n$ th-order NHSE have  $O(L^{d-n+1})$  skin states [6,10,14]. However, these states occupy a boundary of codimension  $d - n$ , resulting in a collapse of  $O(L)$  boundary states in the  $(d - n)$ -dimensional boundary.

Recently, experimental observations of the NHSE across various physical platforms have been reported. The first-order NHSE was initially demonstrated in one-dimensional (1D) photonic lattices [15], quantum systems [5,16], topoelectrical circuits [17], mechanical systems [18], and acoustic lattices [19,20]. Higher-order NHSE has also been observed in 2D and 3D systems recently, including topoelectrical circuits [21,22], acoustic lattices [23–25], and active particles

[26]. Nevertheless, all of these experimental observations occurred in square or cubic lattices whose Hamiltonians are separable; that is, they can be written as  $h(k_x, k_y) = h(k_x) \otimes I + I \otimes h(k_y)$ , where  $I$  is the identity matrix [27]. Consequently, their eigenstates take the simple form  $\psi(k_x, k_y) = \psi(k_x) \otimes \psi(k_y)$  with corresponding energies  $E(k_x) + E(k_y)$ , where  $\psi(k_i)$ , for  $i = x, y$ , are the eigenstates to the 1D problem,  $h(k_i)\psi(k_i) = E(k_i)\psi(k_i)$ . Thus, these systems are straightforward extensions of the 1D Hatano-Nelson and/or non-Hermitian Su-Schrieffer-Heeger models to higher dimensions. If the higher-order NHSE is a general feature of non-Hermitian lattices with higher-order topology, it could also arise in nonseparable lattices. However, a systematic approach to thoroughly understand and classify the topological mechanisms that protect these phases remains an open question of topological band theory.

Here, we use the Hermitian–non-Hermitian correspondence [6] to demonstrate that the dimerized kagome lattice with nonreciprocal nearest neighbors exhibits a higher-order non-Hermitian skin effect. The parent Hermitian Hamiltonian of this kagome lattice is the honeycomb lattice with Kekulé distortion, commonly referred to as the “breathing honeycomb” lattice, which has been shown to exhibit a higher-order topological insulator (HOTI) phase protected by chiral and crystalline symmetries [28]. Unlike previous models [29], the particular non-Hermitian kagome lattice resulting from this correspondence does not require long-range hoppings, making its realization far more feasible. We then experimentally verify this effect in a non-Hermitian acoustic kagome lattice composed of cavities interconnected in a nonreciprocal (unidirectional) manner.

Topological acoustics is a versatile platform for realizing various types of topological phases, including those exhibiting

\*These authors contributed equally to this work.

†Contact author: lujing@nju.edu.cn

‡Contact author: yqj5201@psu.edu

§Contact author: benalcazar@emory.edu

the NHSE [19,23]. While the NHSE can be realized in passive acoustic lattices through intentionally induced losses, it is often significantly obscured by the substantial loss [20,23,30]. Previous studies have shown that it is notably more flexible and straightforward to observe the NHSE in an active acoustic lattice by introducing gain [19,31,32]. In these existing active acoustic lattices, reciprocal hoppings are provided by physically connected passive components such as tubes, while nonreciprocal hoppings are realized by pairs of sources (e.g., loudspeakers) and detectors (e.g., microphones). In contrast to these acoustic lattices, our implemented lattice features sites interconnected solely by nearest-neighbor unidirectional hopping, thereby simplifying its implementation. Additionally, our platform eliminates the geometric constraints imposed by physically connected passive components, making it easier to implement complex topological networks and to implement periodic boundary conditions. To observe the NHSE, we first intentionally rotate the complex energy spectrum by implementing complex hoppings to minimize the loss of skin states while maintaining the system's stability. Additionally, we implement the complex-frequency excitation (CFE) technique, which was recently reported to provide virtual gain to compensate for the loss in a system without causing stability issues [33–38]. The CFE technique has also been introduced to augment the observation of the NHSE in non-Hermitian acoustic lattices, where much clearer energy localization can be observed due to the compensation for the background loss [20,25]. By combining these techniques, we observe a significant confinement of acoustic energy at a specific corner in the topologically nontrivial phase when sites at the edges are excited—even if the excitation site is located far from that corner. In contrast, the acoustic energy spreads out throughout the bulk when bulk states are excited. Both observations present evidence of a higher-order NHSE, the first one observed in a lattice with a nonseparable 2D Bloch Hamiltonian.

## II. CHIRAL-SYMMETRIC HOTI AND THE HIGHER-ORDER NHSE

We may find systems supporting the higher-order NHSE protected by  $C_n$  symmetry—the symmetry that leaves a crystal invariant upon rotation by  $2\pi/n$  rad—by noting that, for each Hermitian HOTI  $h(\mathbf{k})$  protected by chiral symmetry,

$$\Gamma h(\mathbf{k})\Gamma^{-1} = -h(\mathbf{k}), \quad (1)$$

as well as  $C_{2n}$  symmetry,

$$r_{2n}h(\mathbf{k})r_{2n}^\dagger = h(R_{2n}\mathbf{k}), \quad (2)$$

there is a corresponding non-Hermitian Hamiltonian with the same topological information as  $h(\mathbf{k})$ , obeying  $C_n$  symmetry. In Eq. (1),  $\Gamma$  represents the chiral operator, while in Eq. (2),  $r_{2n}$  is the unitary  $C_{2n}$  rotation operator and  $R_{2n}$  is the rotation matrix of the momentum vector  $\mathbf{k}$  by an angle  $\pi/n$ , both satisfying  $(r_{2n})^{2n} = I_{2N \times 2N}$  and  $(R_{2n})^{2n} = I_{2 \times 2}$ , where the unit cell of the crystal has  $2N$  degrees of freedom.

For Hermitian systems, chiral symmetry (1) is equivalent to sublattice symmetry. Consequently, one can always choose a basis where the chiral operator is  $\Gamma = \sigma_z \otimes I_N$ , making the

Bloch Hamiltonian take the off-diagonal form

$$h(\mathbf{k}) = \begin{pmatrix} 0 & q(\mathbf{k}) \\ q^\dagger(\mathbf{k}) & 0 \end{pmatrix}, \quad (3)$$

where  $q(\mathbf{k})$  is generally a non-Hermitian  $N \times N$  matrix. In the basis in which the Hamiltonian in Eq. (3) is written,  $r_{2n}$  is block diagonal,

$$r_{2n} = \begin{pmatrix} r_n & 0 \\ 0 & r_n \end{pmatrix}, \quad \text{where } r_n q(\mathbf{k}) r_n^\dagger = q(R_n \mathbf{k}). \quad (4)$$

Reference [39] has shown that under the symmetry conditions (1) and (2), Hamiltonians of the form in Eq. (3) having corner-induced filling anomalies host corner-localized zero-energy states.

Here, we observe that all the information of  $h(\mathbf{k})$  is contained in the block  $q(\mathbf{k})$ , which possesses  $C_n$  symmetry [see Eq. (4)]. The Hermitian–non-Hermitian correspondence involves interpreting  $q(\mathbf{k})$  as a non-Hermitian Hamiltonian in its own right. Since both  $h(\mathbf{k})$  and  $q(\mathbf{k})$  carry the same topological information, Hermitian Hamiltonians  $h(\mathbf{k})$  describing chiral symmetric HOTIs with higher-order boundary states will have a non-Hermitian counterpart  $q(\mathbf{k})$  with nontrivial higher-order topology and higher-order boundary states. One can visualize the connection between chiral zero-energy states in  $h(\mathbf{k})$  and skin states in  $q(\mathbf{k})$  by noting that the chiral zero-energy states of a bipartite Hamiltonian, such as Eq. (3), are supported on one sublattice and, for that reason, are also exponentially localized eigenstates of  $q(\mathbf{k})$  or  $q^\dagger(\mathbf{k})$  with zero energy. See Supplemental Note S1 for a more detailed discussion in one dimension [40].

In the following, we apply the Hermitian–non-Hermitian correspondence to the 2D breathing honeycomb lattice [28], a gapped Hermitian lattice with zero-energy corner states protected by chiral and  $C_6$  (and thus  $C_3$ ) symmetries, to define a non-Hermitian kagome lattice supporting a second-order NHSE protected by  $C_3$  symmetry. It should be emphasized that the theoretical framework here is generic and, therefore, can be applied to other lattices.

### A. Correspondence of Hermitian breathing honeycomb and non-Hermitian kagome models

The breathing honeycomb model consists of a 2D triangular Bravais lattice where each unit cell has six sites arranged in a hexagon [see Fig. 1(a)]. The tight-binding model (TBM) contains nearest-neighbor hopping terms with strength  $\kappa_{\text{intra}}$  between sites within the same unit cell and intercell nearest-neighbor hoppings with strength  $\kappa_{\text{inter}}$ , giving rise to six energy bands. Due to the model's chiral (sublattice) symmetry, the three lower bands lie below the zero energy level, while the upper bands are reflections of the first three about  $E = 0$ . In Fig. 1(a), we distinguish the two sublattices by their color—white or green.

In addition to chiral symmetry, the breathing honeycomb model possesses time-reversal symmetry (TRS) and belongs to class BDI in the 10-fold classification of Hermitian Hamiltonians [41]. This class does not exhibit nontrivial topological phases at first order in two dimensions. However, the additional  $C_6$  symmetry protects second-order topological zero

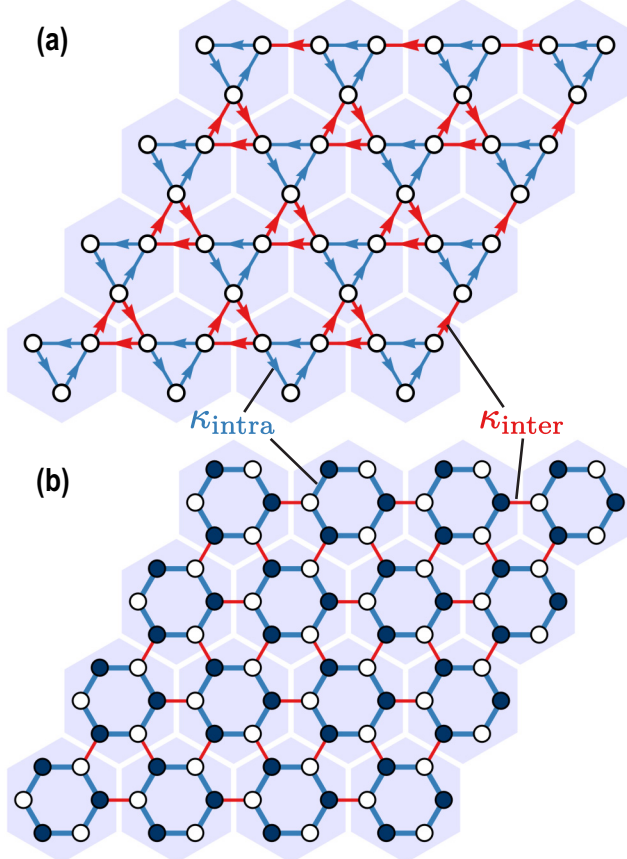


FIG. 1. Hermitian HOTI and its non-Hermitian counterpart. (a) The non-Hermitian kagome lattice, where all hoppings are unidirectional. (b) The Hermitian breathing honeycomb lattice, where all hoppings are reciprocal. The intra- (red) and intercell (blue) hoppings are denoted by  $\kappa_{\text{intra}}$  and  $\kappa_{\text{inter}}$ , respectively. For simplicity, their ratio is defined as  $\kappa = \kappa_{\text{intra}}/\kappa_{\text{inter}}$ .

energy states at specific corners of the lattice when  $\kappa \equiv \kappa_{\text{intra}}/\kappa_{\text{inter}} < 1$  [28].

The presence of chiral symmetry allows us to express the breathing honeycomb's  $6 \times 6$  Bloch Hamiltonian in the off-diagonal form Eq. (3), with the  $3 \times 3$  non-Hermitian block  $q(\mathbf{k})$  given by

$$q(\mathbf{k}) = \begin{pmatrix} 0 & \kappa_{\text{intra}} & \kappa_{\text{inter}} e^{i\mathbf{k} \cdot \mathbf{a}_1} \\ \kappa_{\text{inter}} e^{i\mathbf{k} \cdot \mathbf{a}_2} & 0 & \kappa_{\text{intra}} \\ \kappa_{\text{intra}} & \kappa_{\text{inter}} e^{i\mathbf{k} \cdot \mathbf{a}_3} & 0 \end{pmatrix}. \quad (5)$$

Here,  $\mathbf{a}_1 = (1, 0)$ ,  $\mathbf{a}_2 = -(1/2, \sqrt{3}/2)$ ,  $\mathbf{a}_3 = (-1/2, \sqrt{3}/2)$  are primitive lattice vectors connecting neighboring unit cells.

When taken as a non-Hermitian Hamiltonian, the matrix  $q(\mathbf{k})$  in Eq. (5) describes a non-Hermitian Bloch Hamiltonian on a kagome lattice, consisting of a triangular lattice of unit cells, each having three sites, and where the nearest-neighbor hoppings are unidirectional, having strengths  $\kappa_{\text{intra}}$  (for intracell hoppings) and  $\kappa_{\text{inter}}$  (for intercell hoppings) as shown in Fig. 1(b). The Bloch Hamiltonian in Eq. (5) satisfies the

$C_3$  symmetry condition

$$r_3 q(\mathbf{k}) r_3^\dagger = q(R_3 \mathbf{k}), \quad (6)$$

where  $R_3$  is the rotation matrix by an angle  $2\pi/3$ , and  $r_3 = \begin{pmatrix} 0 & 1 & 0 \\ 0 & 0 & 1 \\ 1 & 0 & 0 \end{pmatrix}$  is the  $C_3$  rotation operator. Additionally,  $q(\mathbf{k})$  is time-reversal symmetric:  $\Theta q(\mathbf{k}) \Theta^{-1} = q(-\mathbf{k})$ , where  $\Theta$  represents complex conjugation for our spinless model. However, it is important to note that for non-Hermitian Hamiltonians, there is a ramification of TRS into an additional symmetry condition,  $\Theta q^\dagger(\mathbf{k}) \Theta^{-1} = q(-\mathbf{k})$  [42], and that  $q(\mathbf{k})$  violates this condition.

Analogous to its Hermitian counterpart,  $q(\mathbf{k})$  falls into symmetry class AI in the 38-fold classification for non-Hermitian Hamiltonians [42]. This class has a winding number of zero in 2D, indicating that our system does not host the first-order NHSE. However, the presence of crystalline symmetries, specifically  $C_3$  in this case, enriches the 38-fold classification, resulting in higher-order topological phases that exhibit the higher-order NHSE.

## B. Topological phases and bulk topological invariants

We can distinguish the topological phases of non-Hermitian Hamiltonians protected by  $C_3$  symmetry through the irreducible representations that the eigenstates take at high-symmetry points (HSPs) of the Brillouin zone  $\Pi = \mathbf{K}, \mathbf{K}', \Gamma$  [Fig. 2(a)]. These three HSPs obey  $R_3 \Pi = \Pi$  modulo a reciprocal-lattice vector, and  $C_3$  symmetry [Eq. (6)] implies  $[r_3, q(\Pi)] = 0$ . Therefore, the eigenstates of the energy band  $m$  at the HSPs, which satisfy  $q(\Pi) |\varepsilon_m(\Pi)\rangle = \varepsilon_m(\Pi) |\varepsilon_m(\Pi)\rangle$ , are also the eigenstates of the rotation operator,  $r_3 |\varepsilon_m(\Pi)\rangle = \Pi_p^{(3)} |\varepsilon_m(\Pi)\rangle$ . For spinless systems, the  $C_3$  rotation operator satisfies  $r_3^3 = 1$ , and the rotation eigenvalues are  $\Pi_1^{(3)} = 1$ ,  $\Pi_2^{(3)} = e^{2\pi i/3}$ ,  $\Pi_3^{(3)} = e^{-2\pi i/3}$ . The  $\Pi_{p=1,2,3}^{(3)}$  eigenvalues label the  $C_3$  symmetry representations of the eigenstates at the various HSPs. If the eigenvalues within the same band differ for distinct HSPs, the energy band has a nontrivial topology. If they are all the same, the topology is trivial. For a formal definition and evaluation of the topological indices that characterize the two phases of the non-Hermitian kagome Hamiltonian (5), see Supplemental Note S2 [40].

The non-Hermitian Hamiltonian in Eq. (5) has two phases that can be accessed depending on the ratio  $\kappa = \kappa_{\text{intra}}/\kappa_{\text{inter}}$ . For  $\kappa < 1$ , as shown in Fig. 2(b), the  $C_3$  representations at the three HSPs  $\Gamma$ ,  $\mathbf{K}$ , and  $\mathbf{K}'$  are all different within the same band, signaling a nontrivial phase. At  $\kappa = 1$ , when the intra- and intercell hopping strengths are equal, the three bands touch at the HSPs, becoming twofold-degenerate [Fig. 2(c)]. For  $\kappa > 1$ , the symmetry representations are exchanged [compare Figs. 2(b) and 2(d)], so that now all  $C_3$  eigenvalues within the same band are the same, indicating a trivial phase.

## C. Winding numbers of counterpropagating edge bands under partial PBC

Although the winding number of the bulk spectrum is zero, the nontrivial topological phase ( $\kappa < 1$ ), protected by line

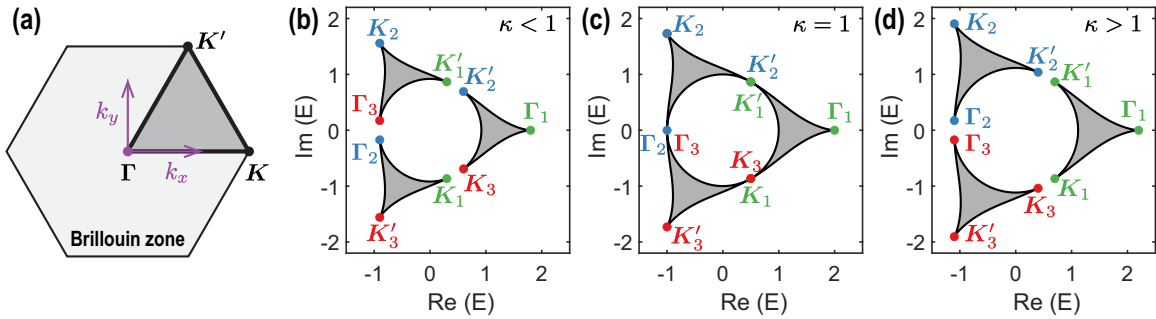


FIG. 2. (a) Brillouin zone for the non-Hermitian kagome lattice showing the locations of the HSPs  $\Gamma = (0, 0)$ ,  $K = (4\pi/3, 0)$ , and  $K' = (2\pi/3, 2\pi/\sqrt{3})$ . (b)–(d) Representations of  $C_3$  symmetry for bulk states at the Brillouin zone points  $K$ ,  $K'$ , and  $\Gamma$  in the (b) topological phase, (c) transition point, and (d) trivial phase. The respective parameters are  $\kappa = 0.8$ ,  $\kappa = 1$ , and  $\kappa = 1.2$ . Green (●), blue (●), and red (●) dots represent the values  $\Pi_1^{(3)} = 1$ ,  $\Pi_2^{(3)} = e^{2\pi i/3}$ , and  $\Pi_3^{(3)} = e^{-2\pi i/3}$ , respectively.

gaps that close at  $\kappa = 1$ , supports two edge-localized bands with opposite winding numbers relative to a point gap at the origin of the complex plane. These bands arise when we open the boundaries along one direction, say  $x$  with length  $L_x$ , while keeping periodic boundary conditions (PBCs) along the  $y$ -direction, with length  $L_y$ . In this configuration, the eigenstates can be localized in the  $x$ -direction while maintaining translation invariance along the  $y$ -direction, and they are labeled by a one-dimensional crystal momentum  $k_y \in (0, 4\pi/\sqrt{3})$ .

Figures 3(b) and 3(c) show the energy spectrum of the non-Hermitian kagome lattice under partial PBC [illustrated in Fig. 3(a)] in the topological phase  $\kappa < 1$ . The boundary and bulk states are presented in Supplemental Fig. S1 [40]. In addition to the three bulk bands, there are two circles of complex energies with opposite winding in  $k_y$ -space. The inner circle consists of  $L_y$  eigenstates exponentially localized at the left boundary of the system ( $x = 1$ ), while the outer circle corresponds to  $2L_y$  eigenstates located at the right boundary ( $x = L_x$ ). We can see that the right boundary has twice as many states as the left boundary. In the inner circle, there is one state for each value of  $k_y$ , and as  $k_y$  spans the Brillouin zone, the total set of  $L_y$  states in that circumference winds counterclockwise around the point gap, resulting in a winding number  $w = +1$ . On the other hand, there are two states on the outer circle for each value of  $k_y$ , forming two semicircles with  $L_y$  states each. Both semicircles half-wind clockwise around the origin as  $k_y$  sweeps the Brillouin zone, resulting in a total winding number  $w = -1$  for the outer circle.

Additionally, since the total winding number must always be zero by the 38-fold classification, one edge band cannot merge into the bulk while the other remains gapped. This is particularly clear in Fig. 3(c), where the boundary states of the outer circle (green) “wait” for the coming of the inner circle (red) before overlapping with the bulk bands. As shown in Fig. 3(d), both circles hybridize and disappear simultaneously at  $\kappa = 1$ , when the line gaps close but the point gap remains open. For  $\kappa > 1$ , only the three trivial bulk bands remain [see Fig. 3(e)].

Crucially, in the topological phase, the boundary at  $x = 1$  ( $x = L_x$ ) acts as a 1D Hatano-Nelson chain under PBC that favors motion in the negative (positive)  $y$  direction. If we had partial PBC along the  $x$  direction, the edge bands would localize at  $y = 1$  and  $y = L_y$ , favoring motion in the positive and negative  $x$  directions, respectively.

#### D. Spectrum under OBC and corner skin states

Under full open boundary conditions (OBCs), the lattice takes the shape of a parallelogram [see Fig. 4(a)] with sides  $L_x = L_y = L$ , allowing the eigenstates to be localized in both the  $x$ - and  $y$ -directions. The corresponding spectrum in the nontrivial phase is displayed in Fig. 4(b).

The states that were previously located on opposite edges, forming two rings under partial PBC, are now all exponentially localized within the same spatial region. This is illustrated in Fig. 4(c), which shows the local density of states (LDOS) per unit cell, defined as the sum of the squared amplitudes of the eigenstates over the three sites within each unit cell. Therefore, these corner skin states may hybridize and give rise to a single circular structure with three small line gaps, resulting in a zero winding number relative to the origin, in accordance with the constraints imposed by the model’s symmetry class. Figure 4(d) shows the LDOS of the bulk bands for comparison.

Upon examining Fig. 4(c), one can observe that the skin states of the non-Hermitian Hamiltonian  $q(\mathbf{k})$  in (5) are all localized at the top left corner of the lattice. If we were to consider its Hermitian conjugate  $q^\dagger(\mathbf{k})$ , the skin states would instead be localized at the bottom right corner. This is not coincidental; their parent Hermitian Hamiltonian (3), which describes a parallelogram-shaped breathing honeycomb lattice, hosts two topologically protected chiral zero energy states—one at the top left corner and the other at the bottom right corner (these states exist at corners with a  $2\pi/3$  angle). In general, the Hermitian–non-Hermitian correspondence predicts that each set of skin states in  $q(\mathbf{k})$  and  $q^\dagger(\mathbf{k})$  originates from a pair of oppositely localized zero-energy states of  $h(\mathbf{k})$ , protected by chiral symmetry.

### III. OBSERVATION OF THE HIGHER-ORDER NHSE IN NON-HERMITIAN ACOUSTIC KAGOME LATTICES

As shown in Fig. 5(a), the experimental platform is a non-Hermitian acoustic kagome lattice with nonreciprocal hoppings and dimensions of  $L_x = L_y = L = 3$ . The photo of the experiment setup is presented as Fig. S2 in the Supplemental Material [40]. The lattice comprises 27 3D-printed hexagonal prism-shaped acoustic cavities, each hosting the first dipole mode with a resonant frequency of 1034.5 Hz in the vertical

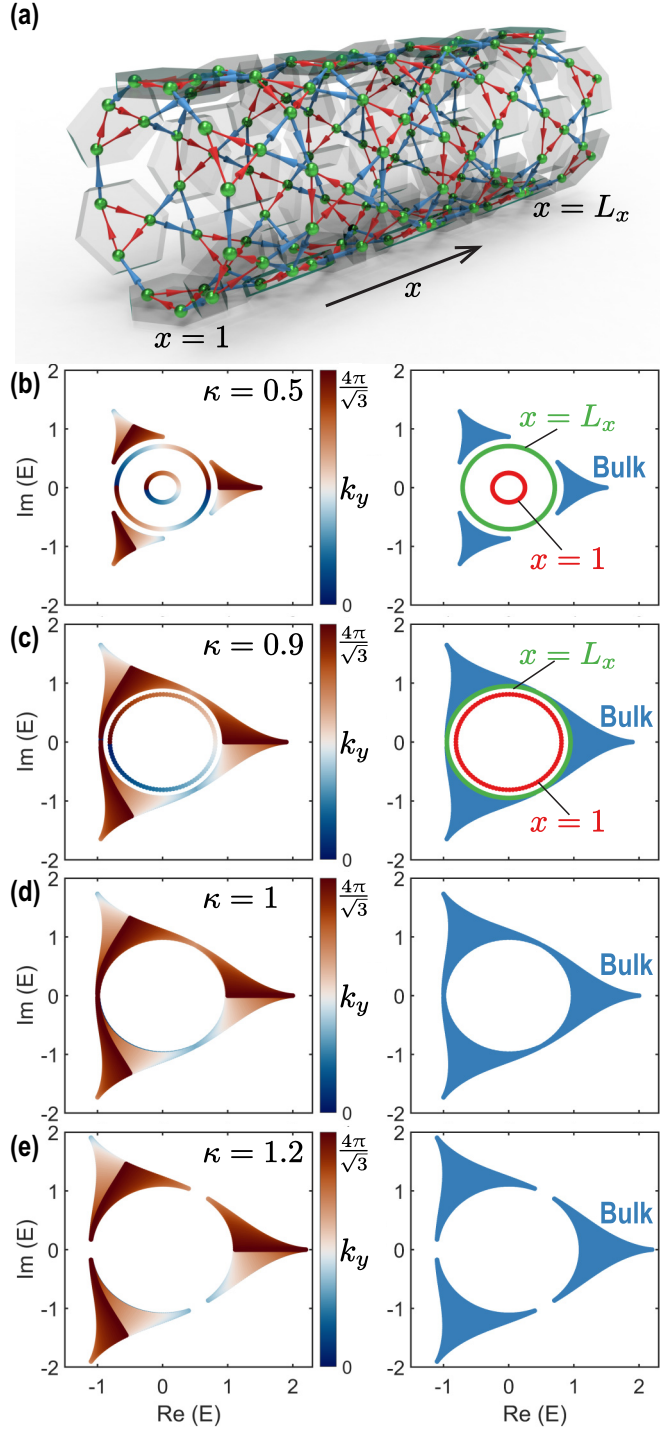


FIG. 3. (a) Schematic of the non-Hermitian kagome lattice with OBC in the  $x$ -direction and PBC in the  $y$ -direction. Here, the first and last unit cells in the  $y$ -direction of the lattice are connected to form a ring. (b)–(e) Energy spectra for (b)  $\kappa = 0.5$ , (c)  $\kappa = 0.9$ , (d)  $\kappa = 1$ , and (e)  $\kappa = 1.2$ . The left column shows the value of  $k_y$  of the corresponding eigenstates through the color gradient, which spans the first Brillouin zone ( $0, \frac{4\pi}{\sqrt{3}}$ ) in the  $y$ -direction. The right column indicates whether a given state is localized at  $x = 1$  (red),  $x = L_x$  (green), or it belongs to the bulk (blue).

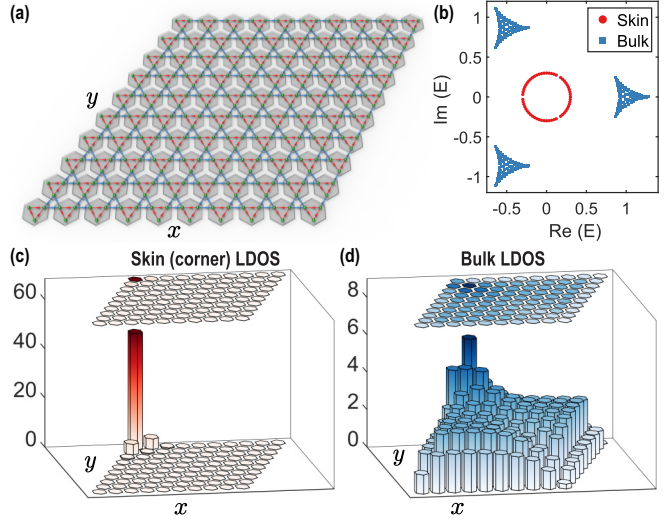


FIG. 4. (a) Schematic of the non-Hermitian kagome lattice with OBCs in both the  $x$ - and  $y$ -directions, with dimensions  $L_x = L_y = 10$ . (b) Energy spectrum with  $\kappa = 0.3$ . Skin (corner) states are in red, while bulk states are in blue. (c) LDOS of skin (corner) states per unit cell. (d) LDOS of bulk states per unit cell.

direction (see Appendix 1 for more details). To form the lattice, the cavities are coupled through loudspeaker (source) and microphone (detector) pairs, enabling unidirectional hopping between nearest-neighbor cavities [see Fig. 5(h)]. The eigenfrequencies in the complex plane, calculated using the TBM and parameters fitted from measurements, are presented in Figs. 5(b) and 5(d) for the nontrivial ( $\kappa = 0.5$ ) and trivial ( $\kappa = 2$ ) cases, respectively. Here, the intra- and intercell hoppings are real-valued,  $\kappa_{\text{intra}}, \kappa_{\text{inter}} \in \mathbb{R}$ , and they are fitted through the measured signals. In the spectrum shown in Fig. 5(b), there is one circumference (red dots) that hosts skin states, all localized at the top left corner [Fig. 5(f)]. The remaining points, denoted by blue squares, host bulk states, which are demonstrated in Fig. 5(g). For the trivial case shown in Fig. 5(d), however, only bulk states exist.

#### A. Acoustic realization of the spectrum rotation technique

It is important to note that when hoppings are real-valued, Figs. 5(b) and 5(d) show that the imaginary part of some states is greater than 0, indicating pure gain at these states. Due to the positive feedback among hoppings in the lattice, the system becomes unstable and tends to crash when any imaginary part is positive. Therefore, to more efficiently observe the higher-order NHSE, we intentionally rotate the spectrum in the complex frequency plane by an angle, which can be either  $-\pi/2$ ,  $\pi/6$ , or  $5\pi/6$  due to  $C_3$  symmetry. This rotation ensures that all states remain below the real axis, thereby maintaining system stability, as illustrated in Figs. 5(c) and 5(e). After the rotation, the imaginary parts of all eigenfrequencies are negative, ensuring system stability, while spatial distributions of skin and bulk states remain the same as shown in Figs. 5(f) and 5(g), respectively. Based on the TBM, it is seen that the spectrum can be rotated by an angle of  $\theta$  with respect to the on-site energy  $\omega_0$  by multiplying both intra- and intercell hoppings with a phase term  $\exp(i\theta)$ , i.e.,

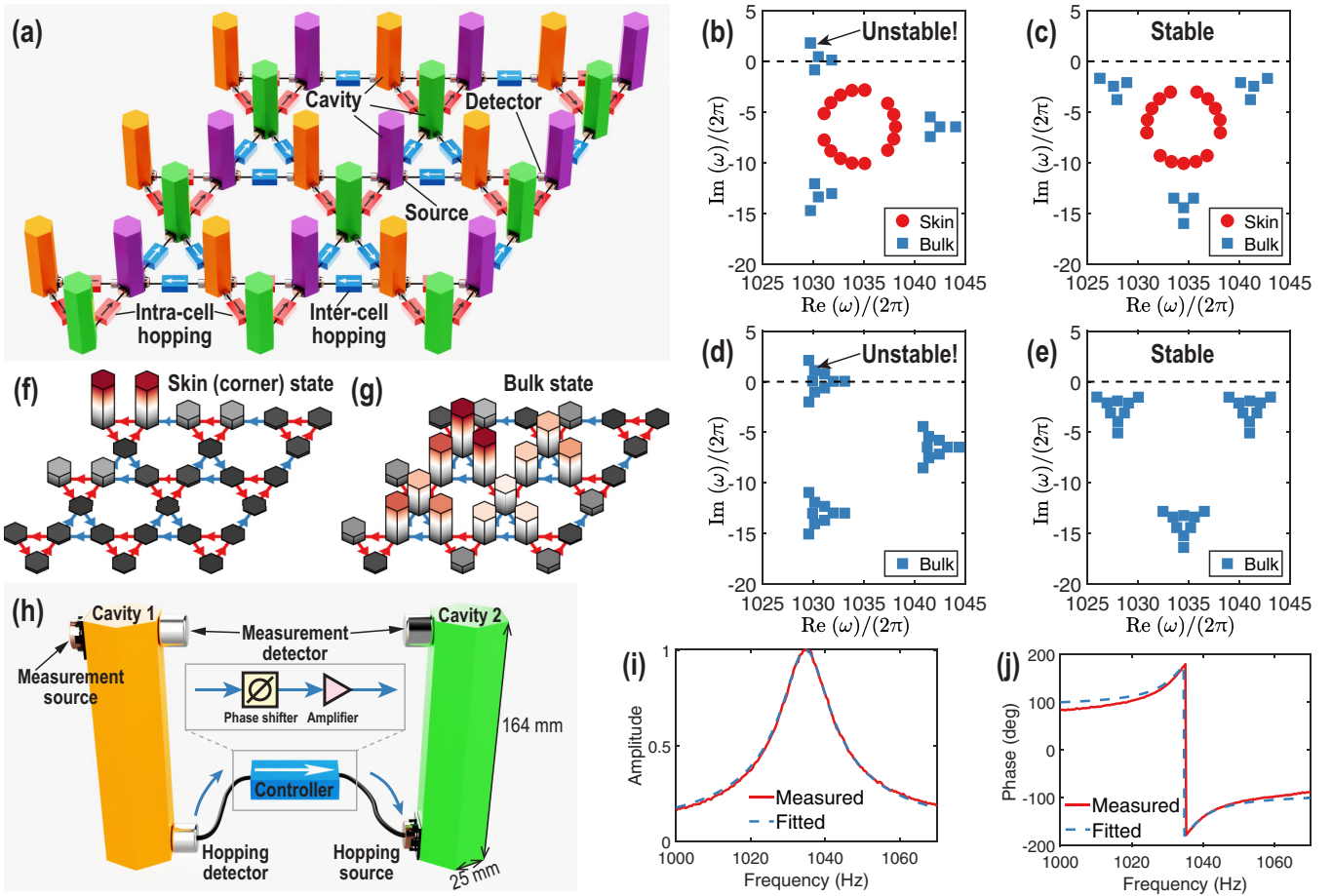


FIG. 5. (a) Schematic of the non-Hermitian acoustic kagome lattice with dimensions  $L_x = L_y = 3$ , where the unidirectional hopping is realized by a source and detector pair, and acoustic cavities are represented by hexagonal prisms. (b,c) Complex eigenfrequencies for the nontrivial lattice obtained using the TBM with  $|\kappa_{\text{inter}}|/(2\pi) = |\kappa_{\text{intra}}|/\pi = 7.43 \text{ Hz}$ . (d,e) Complex eigenfrequencies for the trivial lattice obtained using the TBM with  $|\kappa_{\text{intra}}|/(2\pi) = |\kappa_{\text{inter}}|/\pi = 7.43 \text{ Hz}$ . The phases of both intra- and intercell hoppings are  $\angle\kappa_{\text{intra}} = \angle\kappa_{\text{inter}} = 0$  in (b,d), while they are  $\angle\kappa_{\text{intra}} = \angle\kappa_{\text{inter}} = -\pi/2, \pi/6, \text{ or } 5\pi/6$  in (c,e). Spatial distributions of (f) skin (corner) and (g) bulk states. (h) Schematic of the unidirectional hopping realized by a detector and a source. Experimentally measured and numerically fitted (i) amplitude and (j) phase response of the cross-power spectral density of the acoustic signals measured in cavities 1 and 2 shown in (h).

$\kappa_{\text{intra}} \rightarrow \kappa_{\text{intra}} \exp(i\theta)$  and  $\kappa_{\text{inter}} \rightarrow \kappa_{\text{inter}} \exp(i\theta)$ , while their ratio remains the same,  $\kappa = \kappa_{\text{intra}}/\kappa_{\text{inter}}$ .

To validate the spectrum rotation technique in experiments, we start with a simple coupled acoustic cavity system as shown in Fig. 5(h). The unidirectional hopping is realized by active acoustic components, including a microphone (hopping detector), a loudspeaker (hopping source), an amplifier, and a phase shifter. The microphone is placed in cavity 1 to detect the acoustic pressure inside this cavity. The phase of the detected acoustic pressure is adjusted, the signal is amplified, and then emitted by the loudspeaker placed in cavity 2. The tight-binding Hamiltonian of this system is

$$H_2 = \begin{pmatrix} \omega_0 & 0 \\ \kappa_0 & \omega_0 \end{pmatrix}. \quad (7)$$

Here,  $\kappa_0 \in \mathbb{C}$  is the unidirectional hopping from cavity 1 to cavity 2, which is complex-valued and can be either intra- or intercell hopping. The real and imaginary parts of the on-site energy,  $\omega_0$ , represent the first resonant frequency and the intrinsic loss of a single cavity, respectively. By exciting a single cavity with a loudspeaker and recording the signal using a mi-

crophone, the on-site frequency can be fitted to approximately  $\omega_0/(2\pi) = 1034.5 \text{ Hz} - 6.37i \text{ Hz}$  (see Appendix 1 for more details).

To determine both the amplitude and the phase of the unidirectional hopping  $\kappa_0$  in Eq. (7), we excite at cavity 1 using a loudspeaker [measurement source in Fig. 5(h)] and measure the acoustic pressure in both cavities using two microphones. The cross-power spectral density of these two measured pressure signals can be expressed as  $G(\omega) = \psi_2(\omega)/\psi_1(\omega) = \kappa_0/(\omega - \omega_0)$ , where  $\omega$  is the excitation frequency, and  $\psi_i$  represents the acoustic pressure in cavity  $i$  with  $i = 1, 2$  (see Supplemental Note S3 for details [40]). The spectral response of  $|G(\omega)|$  has a single peak at  $\omega = \text{Re}(\omega_0)$ . Furthermore, when  $\omega = \text{Re}(\omega_0)$ , the phase of  $G$  and  $\kappa_0$  follows the relation

$$\angle G(\text{Re}(\omega_0)) = \angle\kappa_0 - \frac{\pi}{2}. \quad (8)$$

This relation can be used to adjust the phase of  $\kappa_0$  by observing the phase response of  $G(\omega)$ . In the experiment, we set  $\kappa_0$  to  $-\pi/2$ , indicating a counterclockwise rotation of the spectrum by an angle of  $-\pi/2$ , producing the rotated

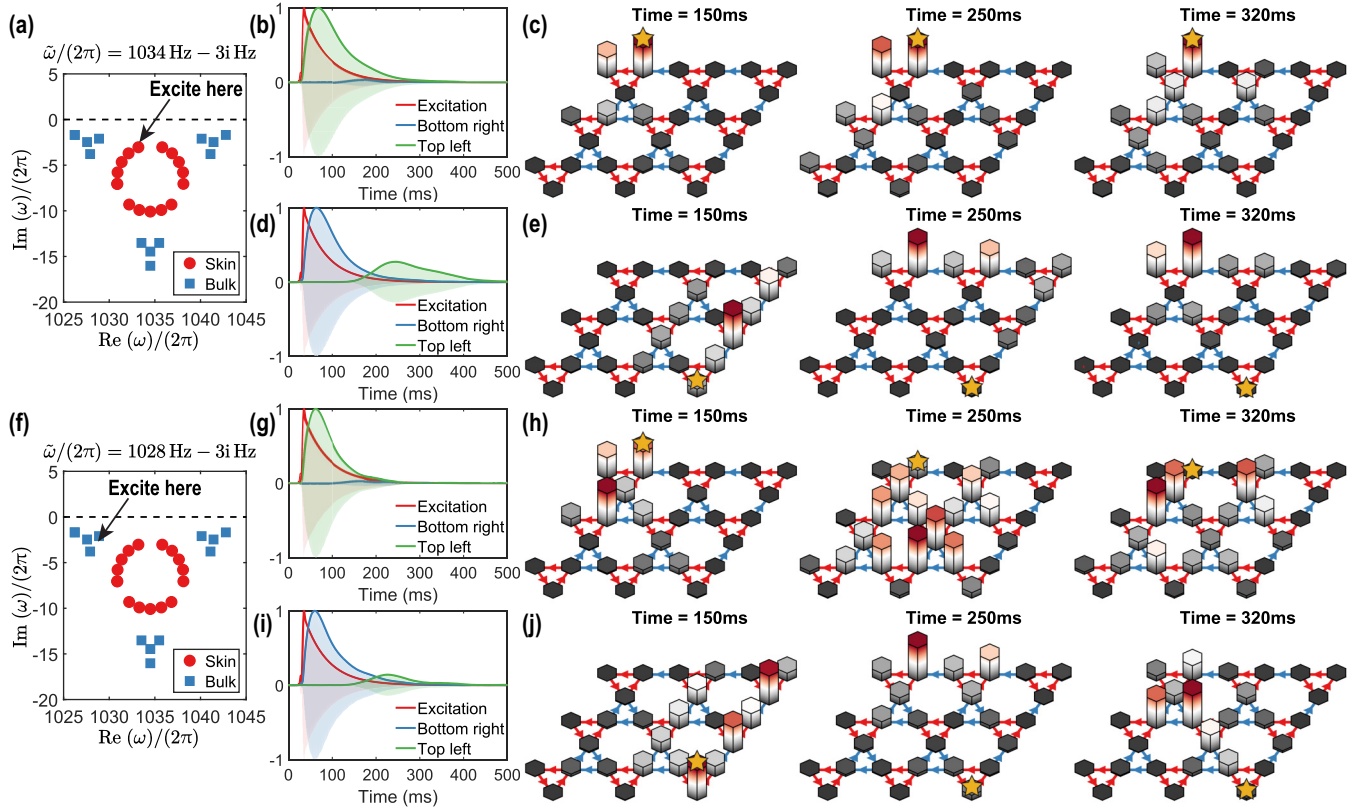


FIG. 6. Experimental demonstration in a nontrivial kagome lattice with dimensions  $L_x = L_y = 3$  and hopping parameters  $\kappa = 0.5$  and  $\kappa_{\text{inter}}/(2\pi) = \kappa_{\text{intra}}/\pi = 7.43e^{-i\pi/2} \text{ Hz}$ . (a,f) The complex eigenfrequencies showing the CFE at (a)  $\tilde{\omega}/(2\pi) = 1034 \text{ Hz} - 3i \text{ Hz}$  and (f)  $\tilde{\omega}/(2\pi) = 1028 \text{ Hz} - 3i \text{ Hz}$ . The lattice is excited by a loudspeaker (denoted by a yellow star  $\star$ ) at a cavity in the (b,c,g,h) top left and (d,e,i,j) bottom right unit cells. (b,d,g,i) The excitation signal and signals measured at the cavity in the top left and bottom right unit cells as a function of time. (c,e,h,j) Acoustic energy distributions measured at 150, 250, and 320 ms.

spectrum shown in Figs. 5(c) and 5(d). Consequently, the phase response of  $G(\omega)$  at  $\omega = \text{Re}(\omega_0)$  should be  $-\pi$  according to Eq. (8). Although analog circuits can be designed to shift the phase of the hopping [31,43–47], they are challenging and time-consuming to adjust precisely for a large lattice. In this work, digital fractional delay filters based on the Lagrange interpolation [48,49] are implemented by a custom-made real-time controller to shift the phase (see Appendixes 2 and 3 for more details). This digital filter approach offers much more precise control of the phase and greater flexibility, especially for adjusting hopping strengths for different topological phases. Figures 5(i) and 5(j) show the amplitude and phase response of  $G(\omega)$ , where measured results agree well with the fitted ones, validating our technique.

### B. Observation of the higher-order NHSE

To observe the higher-order NHSE, we excite the lattice using a loudspeaker at one cavity (denoted by the star in Fig. 6) and measure the acoustic pressure signal at every cavity using a microphone (see Appendix 4 for more details). It is important to note that, to ensure system stability, the imaginary part of the frequencies of the skin states must be negative (indicating physical loss), as shown in Fig. 6(a). Consequently, the observation of the NHSE would be obscured by the loss [20,23]. To address this issue, we adopt the CFE technique

[20,33–38] to observe the NHSE. The CFE technique involves exciting with an exponentially decayed sinusoidal signal in the time domain, where the decay in the signal amplitude introduces an effective virtual gain to compensate for the loss (see Appendix 4 for details). For comparison, the results with traditional real-frequency excitation are presented in Figs. S5 and S6 in the Supplemental Material [40].

For the nontrivial lattice with  $\kappa = 0.5$  as shown in Figs. 6(a) and 6(f), we implement the CFE at  $\tilde{\omega}/(2\pi) = 1034 \text{ Hz} - 3i \text{ Hz}$  and  $1028 \text{ Hz} - 3i \text{ Hz}$ , respectively, to observe the NHSE and bulk states, respectively. Figure 6(b) shows the time evolution of the measured excitation signal and acoustic signals in cavities located in the bottom right and top left unit cells. As observed in both Figs. 6(b) and 6(c), the acoustic energy remains localized at the top left corner most of the time, as expected in Fig. 5(f). When the source is excited at the bottom right unit cell, the time-evolved signals shown in Fig. 6(d) and the spatial distributions of the acoustic energy in Fig. 6(e) demonstrate that the system reaches a stable quasistationary stage after around 250 ms, and the acoustic energy is localized at the top left unit cell, compatible with the transport expected for the NHSE. In this context, the transport response refers to the localization of wave energy to a specific corner, regardless of the excitation location. For comparison,

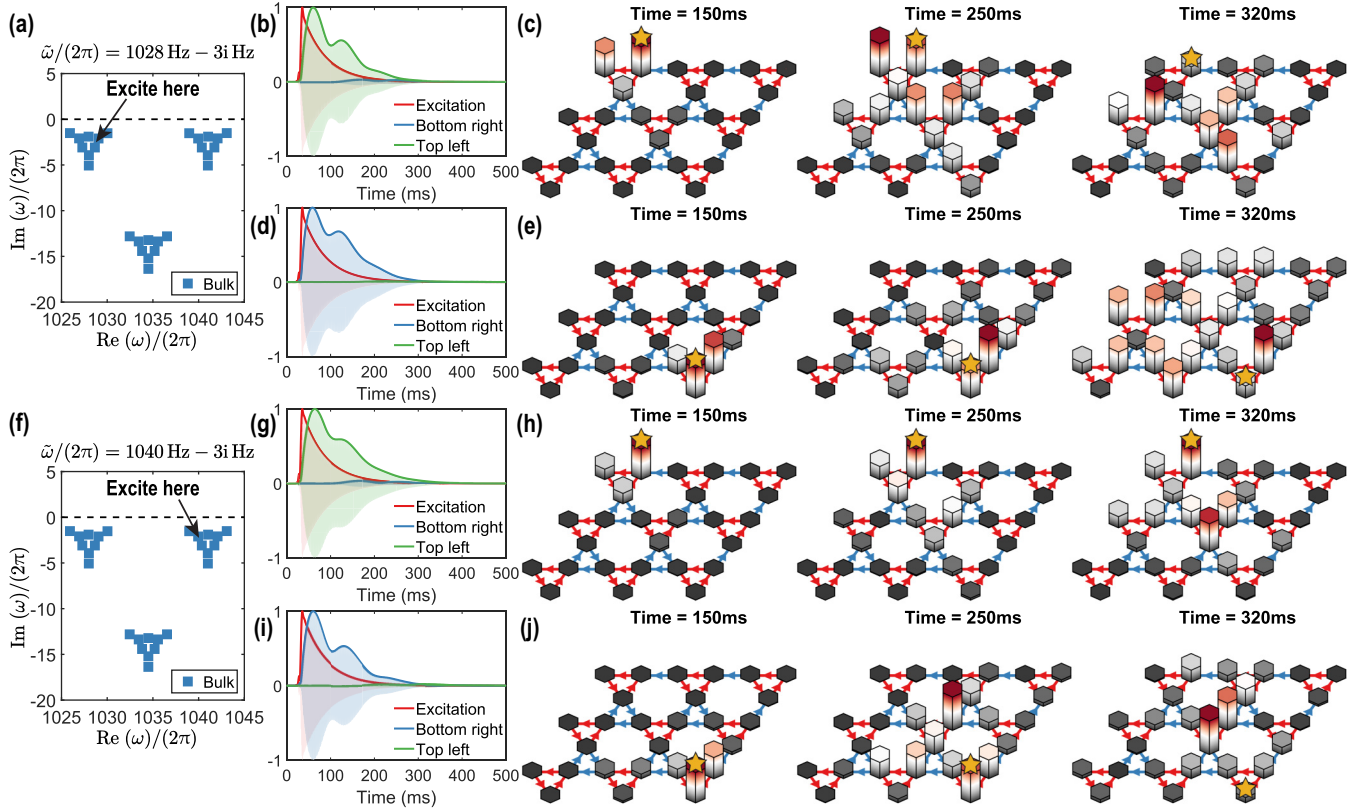


FIG. 7. Experimental demonstration in a trivial kagome lattice with dimensions  $L_x = L_y = 3$  and hopping parameters  $\kappa = 2$  and  $\kappa_{\text{intra}}/(2\pi) = \kappa_{\text{inter}}/\pi = 7.43e^{-i\pi/2}$  Hz. (a,f) The complex eigenfrequencies showing the CFE at (a)  $\tilde{\omega}/(2\pi) = 1034$  Hz  $- 3i$  Hz and (f)  $\tilde{\omega}/(2\pi) = 1028$  Hz  $- 3i$  Hz. The lattice is excited by a loudspeaker (denoted by a yellow star  $\star$ ) at a cavity in the (b,c,g,h) top left and (d,e,i,j) bottom right unit cells. (b,d,g,i) The excitation signal and signals measured at the cavity in the top left and bottom right unit cells as a function of time. (c,e,h,j) Acoustic energy distributions measured at 150, 250, and 320 ms.

as shown in Fig. 6(f), we also measure the time-evolved signals at  $\tilde{\omega}/(2\pi) = 1028$  Hz  $- 3i$  Hz, which is expected to host bulk states. The measured results presented in Figs. 6(g)–6(j) clearly demonstrate that bulk states are excited instead of corner ones. Detailed time evolution of the acoustic energy fields, as well as the excitation at  $\tilde{\omega}/(2\pi) = 1040$  Hz  $- 3i$  Hz hosting bulk states at the other band, are provided as movies and Fig. S3 in the Supplemental Material [40]. For better comparison, we also measure the trivial lattice with  $\kappa = 2$ ; the results are summarized in Fig. 7. The extended data for the trivial lattice are also provided as movies and Fig. S4 in the Supplemental Material [40]. There are only three bulk bands shown in the complex spectrum in Fig. 7(a). We then launch the CFE at 1028 Hz  $- 3i$  Hz and 1040 Hz  $- 3i$  Hz in Figs. 7(a) and 7(f), respectively. The time-evolved signals and the spatial distributions of acoustic energy in Fig. 7 demonstrate the bulk states as expected.

#### IV. DISCUSSION

Through a Hermitian–non-Hermitian correspondence, we identify a recipe for constructing lattices with higher-order NHSE from a HOTI protected by chiral symmetry. Specifically, we construct a non-Hermitian kagome lattice protected by  $C_3$  symmetry from a Hermitian breathing honeycomb

lattice. We also report the experimental observation of the higher-order NHSE in this non-Hermitian acoustic kagome lattice, where nonreciprocity is manifested by the unidirectional amplification of acoustic signals. To minimize the loss of skin states while maintaining system stability, we intentionally rotate the complex spectrum by implementing complex hoppings. Additionally, we utilize the CFE approach, which introduces an effective virtual gain to compensate for the intrinsic loss in the lattice. These techniques allow us to observe the localization of acoustic energy to a corner far away from the excitation location in the topological phase with higher-order NHSE. Our work paves the way for a deeper understanding of higher-order NHSE and potentially innovative applications rooted in acoustic nonreciprocity, such as robust waveguides, nonreciprocal amplifiers [50], and so on [51,52].

#### ACKNOWLEDGMENTS

Y.J. thanks the support of startup funds from Penn State University and NSF awards 2039463 and 1951221. J.L. gratefully acknowledges the financial support by National Natural Science Foundation of China (12274221). W.A.B. gratefully acknowledges the support of startup funds from Emory University.

## APPENDIX: EXPERIMENTAL DETAILS

### 1. Experimental samples

The acoustic cavities used in this work were fabricated using 3D printers with a tolerance of 0.2 mm or within 0.3%. The materials are LEDO 6060 photosensitive resin, which can be considered as acoustically rigid for airborne sound. The printed samples have a thickness of 6 mm. As shown in Fig. 5, all acoustic cavities used in experiments are hexagonal prisms with an interior height of  $l = 164$  mm and a side length of 25 mm. Each acoustic cavity hosts a resonant mode at a frequency of  $c_0/(2l) \approx 1045.7$  Hz, where  $c_0 = 343$  m/s is the airborne sound speed. In the experiments, a loudspeaker (source) is used to excite a single acoustic cavity, and a microphone (detector) is used to measure the acoustic pressure in that cavity. By using the Green's function for a single mode [53],  $\psi(\omega) = -\text{Im}(\omega_0)/(\omega - \omega_0)$ , we retrieve the on-site orbit as  $\omega_0/(2\pi) = 1034.5$  Hz –  $6.37i$  Hz, where  $\omega$  is the excitation frequency.

### 2. Implementation of unidirectional hoppings

As shown in Fig. 5(h), each unidirectional hopping comprises a loudspeaker (CDS-25148-L100, CUI Devices), a microphone (BOB-19389, SparkFun Electronics), and an audio amplifier (EK1236 module equipped with an onboard LM386 chip). The loudspeaker and microphone are placed at the bottom of each cavity. We design and develop a custom-made digital real-time controller to implement the unidirectional hoppings in our model. This allows more flexible control and scalability relative to existing analog amplifier and phase shifter-based approaches [19,31,32,43,54], which become necessary, particularly to capture transport phenomena across topological phase transitions. The microphone captures the acoustic pressure signal, which is then processed by the controller set to a sampling rate of 80 kHz. In this work, digital fractional delay filters based on the Lagrange interpolation [48,49] are implemented by the controller to shift the phase.

The custom-made digital controller consists of three parts: the core board, the motherboard, and the input/output (IO) board. The core board integrates a field-programmable gate array (FPGA, XC7K325T, Xilinx) and a digital signal processor (DSP, TMS320C6678, Texas Instruments). The motherboard provides power and communication buses to the core and IO boards. The IO board acquires and generates real-time signals. Each IO board supports 16-channel analog inputs and outputs. The input channel employs analog-to-digital converters (ADC, ADC7606B, ADI), and the output channel adopts digital-to-analog converters (DAC, DAC8568, Texas Instruments).

As shown in Fig. 5(h), the unidirectional hopping is realized by active acoustic components, including a microphone (hopping detector), a loudspeaker (hopping source), an amplifier, and a phase shifter. In our experiments, as shown in Fig. 5(a) of the manuscript, ensuring uniformity in the acoustic responses relies on carefully tuning the strengths of the multiple hoppings. We tune each hopping strength individually, following the process illustrated in Fig. 5(h), and we determine the precise hopping strength using the method

presented in Figs. 5(i) and 5(j). To eliminate interference during tuning, all other hoppings are disabled while a specific hopping is being adjusted. This approach ensures that interactions from other hoppings do not affect the tuning process. Once all hoppings have been tuned individually, we enable all hoppings simultaneously and proceed with the measurements.

### 3. Stability control and the energy-spectrum rotation

It is noted that feedback within the entire lattice can make the system unstable at acoustic resonant modes. The physical mechanism behind this is that any states with pure gain can cause the system to crash, inducing unstable positive feedback similar to howling sound effects. As demonstrated in Fig. 5, stability around the working resonant mode at  $\text{Re}(\omega_0)$  can be enhanced by rotating the complex energy spectrum to ensure all imaginary parts are less than zero. While reducing the loss of skin states at the working resonant mode  $\text{Re}(\omega_0)$ , the higher-order harmonic resonant modes of the acoustic cavities,  $j \text{Re}(\omega_0)$ , where  $j = 2, 3, \dots$ , can also introduce stability issue. To address this issue, we use digital notch filters (second-order infinite impulse response filters) implemented by the controller to mitigate the second-, third-, fourth-, and fifth-order resonances at 2069, 3103.5, 4138, and 5172.5 Hz, respectively. The  $Q$  factor of the notch filter is set to 10 in experiments.

### 4. Complex-frequency excitation and measurements

To ensure the imaginary parts of all energies are negative, there is a small background loss across the lattice, as shown in Fig. 5. The loss may obscure the higher-order NHSE to a certain extent [20,23]. To more clearly observe the higher-order NHSE, we apply the CFE technique. To illustrate the basic idea of the CFE, consider a simple lossy 1D wave propagation model with a uniform loss  $\gamma_0 > 0$ , where the signal decays spatially according to  $e^{-\gamma_0 z}$ , with  $z > 0$  being the spatial coordinate. Suppose a source is excited at  $z = 0$  with a signal  $s(t)$  at time  $t$ ; the signal is then expressed in the temporal-spatial domain as  $s(t - z/c_p)e^{-\gamma_0 z}$ , where  $c_p > 0$  is the wave speed. If the excitation signal oscillates at a complex frequency  $\tilde{\omega} = \text{Re}(\tilde{\omega}) + i \text{Im}(\tilde{\omega})$ , it takes the form  $s(t) = e^{-i\tilde{\omega}t}$ . Consequently, the wave field is expressed as  $e^{-i\text{Re}(\tilde{\omega})(t-z/c_p)}e^{\text{Im}(\tilde{\omega})t - [\gamma_0 + \text{Im}(\tilde{\omega})/c_p]z}$  with its magnitude of  $e^{\text{Im}(\tilde{\omega})t - [\gamma_0 + \text{Im}(\tilde{\omega})/c_p]z}$ . Clearly, when  $\text{Im}(\tilde{\omega}) = -\gamma_0 c_p < 0$ , the magnitude of the wave field becomes independent of the spatial coordinate  $z$ . A negative imaginary part of  $\tilde{\omega}$ , i.e.,  $\text{Im}(\tilde{\omega}) < 0$ , represents a decaying signal in the time domain, effectively providing a virtual gain to compensate for the spatial loss in the medium.

In experiments, the CFE signal is a two-second sinusoidal signal with an exponential decaying rate in amplitude, with expression  $s(t) = \sin[\text{Re}(\tilde{\omega})t]e^{\text{Im}(\tilde{\omega})t}[u(t) - u(t - 2)]$ , where  $u(t)$  is the Heaviside function. All signals are generated, acquired, and postprocessed by a generator module (B&K Type 3160-A-042 equipped with a LAN-XI panel Type UA-2102-042). The excitation signal is generated from the generator module and drives a loudspeaker (CMS-15118D-L100, CUI Devices) at the top of a cavity. The acoustic pressure is measured by 1/4-in. condenser microphones (B&K Type 4187

equipped with a preamplifier Type 2670) in the receiver cavity. The acoustic spectral response was obtained using the “H1

frequency response” settings in the B&K PULSE LabShop software.

- [1] V. M. Martinez Alvarez, J. E. Barrios Vargas, and L. E. F. Foa Torres, Non-Hermitian robust edge states in one dimension: Anomalous localization and eigenspace condensation at exceptional points, *Phys. Rev. B* **97**, 121401(R) (2018).
- [2] S. Yao and Z. Wang, Edge states and topological invariants of non-Hermitian systems, *Phys. Rev. Lett.* **121**, 086803 (2018).
- [3] F. K. Kunst, E. Edvardsson, J. C. Budich, and E. J. Bergholtz, Biorthogonal bulk-boundary correspondence in non-Hermitian systems, *Phys. Rev. Lett.* **121**, 026808 (2018).
- [4] Z. Yang, K. Zhang, C. Fang, and J. Hu, Non-Hermitian bulk-boundary correspondence and auxiliary generalized Brillouin zone theory, *Phys. Rev. Lett.* **125**, 226402 (2020).
- [5] L. Xiao, T. Deng, K. Wang, G. Zhu, Z. Wang, W. Yi, and P. Xue, Non-Hermitian bulk-boundary correspondence in quantum dynamics, *Nat. Phys.* **16**, 761 (2020).
- [6] K. Kawabata, M. Sato, and K. Shiozaki, Higher-order non-Hermitian skin effect, *Phys. Rev. B* **102**, 205118 (2020).
- [7] W. A. Benalcazar, B. A. Bernevig, and T. L. Hughes, Quantized electric multipole insulators, *Science* **357**, 61 (2017).
- [8] F. Schindler, A. M. Cook, M. G. Vergniory, Z. Wang, S. S. P. Parkin, B. A. Bernevig, and T. Neupert, Higher-order topological insulators, *Sci. Adv.* **4**, eaat0346 (2018).
- [9] C. H. Lee, L. Li, and J. Gong, Hybrid higher-order skin-topological modes in nonreciprocal systems, *Phys. Rev. Lett.* **123**, 016805 (2019).
- [10] R. Okugawa, R. Takahashi, and K. Yokomizo, Second-order topological non-Hermitian skin effects, *Phys. Rev. B* **102**, 241202(R) (2020).
- [11] Y. Fu, J. Hu, and S. Wan, Non-Hermitian second-order skin and topological modes, *Phys. Rev. B* **103**, 045420 (2021).
- [12] X. Zhang, T. Zhang, M.-H. Lu, and Y.-F. Chen, A review on non-Hermitian skin effect, *Adv. Phys.: X* **7**, 2109431 (2022).
- [13] R. Lin, T. Tai, L. Li, and C. H. Lee, Topological non-Hermitian skin effect, *Front. Phys.* **18**, 53605 (2023).
- [14] J. Lu, W. Deng, X. Huang, M. Ke, and Z. Liu, Non-Hermitian topological phononic metamaterials, *Adv. Mater.* **23**07998 (2023).
- [15] S. Weidemann, M. Kremer, T. Helbig, T. Hofmann, A. Stegmaier, M. Greiter, R. Thomale, and A. Szameit, Topological funneling of light, *Science* **368**, 311 (2020).
- [16] Q. Liang, D. Xie, Z. Dong, H. Li, H. Li, B. Gadway, W. Yi, and B. Yan, Dynamic signatures of non-Hermitian skin effect and topology in ultracold atoms, *Phys. Rev. Lett.* **129**, 070401 (2022).
- [17] T. Helbig, T. Hofmann, S. Imhof, M. Abdelghany, T. Kiessling, L. W. Molenkamp, C. H. Lee, A. Szameit, M. Greiter, and R. Thomale, Generalized bulk-boundary correspondence in non-Hermitian topoelectrical circuits, *Nat. Phys.* **16**, 747 (2020).
- [18] A. Ghatak, M. Brandenbourger, J. van Wezel, and C. Coulais, Observation of non-Hermitian topology and its bulk-edge correspondence in an active mechanical metamaterial, *Proc. Natl. Acad. Sci. USA* **117**, 29561 (2020).
- [19] L. Zhang, Y. Yang, Y. Ge, Y.-J. Guan, Q. Chen, Q. Yan, F. Chen, R. Xi, Y. Li, D. Jia, S.-Q. Yuan, H.-X. Sun, H. Chen, and B. Zhang, Acoustic non-Hermitian skin effect from twisted winding topology, *Nat. Commun.* **12**, 6297 (2021).
- [20] Z. Gu, H. Gao, H. Xue, J. Li, Z. Su, and J. Zhu, Transient non-Hermitian skin effect, *Nat. Commun.* **13**, 7668 (2022).
- [21] D. Zou, T. Chen, W. He, J. Bao, C. H. Lee, H. Sun, and X. Zhang, Observation of hybrid higher-order skin-topological effect in non-Hermitian topoelectrical circuits, *Nat. Commun.* **12**, 7201 (2021).
- [22] B. Liu, Y. Li, B. Yang, X. Shen, Y. Yang, Z. H. Hang, and M. Ezawa, Experimental observation of non-Hermitian higher-order skin interface states in topological electric circuits, *Phys. Rev. Res.* **5**, 043034 (2023).
- [23] X. Zhang, Y. Tian, J.-H. Jiang, M.-H. Lu, and Y.-F. Chen, Observation of higher-order non-Hermitian skin effect, *Nat. Commun.* **12**, 5377 (2021).
- [24] Q. Zhang, Y. Leng, L. Xiong, Y. Li, K. Zhang, L. Qi, and C. Qiu, Construction and observation of flexibly controllable high-dimensional non-Hermitian skin effects, *Adv. Mater.* **36**, 2403108 (2024).
- [25] H. Gao, W. Zhu, H. Xue, G. Ma, and Z. Su, Controlling acoustic non-Hermitian skin effect via synthetic magnetic fields, *Appl. Phys. Rev.* **11**, 031410 (2024).
- [26] L. S. Palacios, S. Tchoumakov, M. Guix, I. Pagonabarraga, S. Sánchez, and A. G. Grushin, Guided accumulation of active particles by topological design of a second-order skin effect, *Nat. Commun.* **12**, 4691 (2021).
- [27] Y. Wang, Y. Ke, Y.-J. Chang, Y.-H. Lu, J. Gao, C. Lee, and X.-M. Jin, Constructing higher-order topological states in higher dimensions, *Phys. Rev. B* **104**, 224303 (2021).
- [28] J. Noh, W. A. Benalcazar, S. Huang, M. J. Collins, K. P. Chen, T. L. Hughes, and M. C. Rechtsman, Topological protection of photonic mid-gap defect modes, *Nat. Photon* **12**, 408 (2018).
- [29] L.-W. Wang, Z.-K. Lin, and J.-H. Jiang, Non-Hermitian topological phases and skin effects in kagome lattices, *Phys. Rev. B* **108**, 195126 (2023).
- [30] W. Wang, M. Hu, X. Wang, G. Ma, and K. Ding, Experimental realization of geometry-dependent skin effect in a reciprocal two-dimensional lattice, *Phys. Rev. Lett.* **131**, 207201 (2023).
- [31] X. Wang, W. Wang, and G. Ma, Extended topological mode in a one-dimensional non-Hermitian acoustic crystal, *AAPPS Bull.* **33**, 23 (2023).
- [32] W. Wang, X. Wang, and G. Ma, Non-Hermitian morphing of topological modes, *Nature (London)* **608**, 50 (2022).
- [33] H. Li, A. Mekawy, A. Krasnok, and A. Alù, Virtual parity-time symmetry, *Phys. Rev. Lett.* **124**, 193901 (2020).
- [34] S. Kim, S. Lepeshov, A. Krasnok, and A. Alù, Beyond bounds on light scattering with complex frequency excitations, *Phys. Rev. Lett.* **129**, 203601 (2022).
- [35] S. Kim, Y.-G. Peng, S. Yves, and A. Alù, Loss compensation and superresolution in metamaterials with excitations at complex frequencies, *Phys. Rev. X* **13**, 041024 (2023).
- [36] F. Guan, X. Guo, K. Zeng, S. Zhang, Z. Nie, S. Ma, Q. Dai, J. Pendry, X. Zhang, and S. Zhang, Overcoming losses in superlenses with synthetic waves of complex frequency, *Science* **381**, 766 (2023).

- [37] F. Guan, X. Guo, S. Zhang, K. Zeng, Y. Hu, C. Wu, S. Zhou, Y. Xiang, X. Yang, Q. Dai, and S. Zhang, Compensating losses in polariton propagation with synthesized complex frequency excitation, *Nat. Mater.* **23**, 506 (2024).
- [38] K. Zeng, C. Wu, X. Guo, F. Guan, Y. Duan, L. L. Zhang, X. Yang, N. Liu, Q. Dai, and S. Zhang, Synthesized complex-frequency excitation for ultrasensitive molecular sensing, *eLight* **4**, 1 (2024).
- [39] W. A. Benalcazar, T. Li, and T. L. Hughes, Quantization of fractional corner charge in  $C_n$ -symmetric higher-order topological crystalline insulators, *Phys. Rev. B* **99**, 245151 (2019).
- [40] See Supplemental Material at <http://link.aps.org/supplemental/10.1103/PhysRevB.111.014314> for detailed discussions on the correspondence between zero-energy states of chiral-symmetric Hermitian systems and the skin effect in non-Hermitian systems; topological invariants of  $C_n$ - and time-reversal-symmetric non-Hermitian lattices; the coupled-model theory for unidirectional coupling of two acoustic cavities; a photo of the experimental setup; additional experimental results including both complex and real frequency excitations; and animations depicting the time-evolution of the acoustic field under complex frequency excitation. The Supplemental Material also contains Refs. [6,55,56].
- [41] A. Altland and M. R. Zirnbauer, Nonstandard symmetry classes in mesoscopic normal-superconducting hybrid structures, *Phys. Rev. B* **55**, 1142 (1997).
- [42] K. Kawabata, K. Shiozaki, M. Ueda, and M. Sato, Symmetry and topology in non-Hermitian physics, *Phys. Rev. X* **9**, 041015 (2019).
- [43] Q. Zhang, Y. Li, H. Sun, X. Liu, L. Zhao, X. Feng, X. Fan, and C. Qiu, Observation of acoustic non-Hermitian Bloch braids and associated topological phase transitions, *Phys. Rev. Lett.* **130**, 017201 (2023).
- [44] Q. Zhang, L. Zhao, X. Liu, X. Feng, L. Xiong, W. Wu, and C. Qiu, Experimental characterization of three-band braid relations in non-Hermitian acoustic lattices, *Phys. Rev. Res.* **5**, L022050 (2023).
- [45] Z. Chen, Z. Li, J. Weng, B. Liang, Y. Lu, J. Cheng, and A. Alù, Sound non-reciprocity based on synthetic magnetism, *Sci. Bull.* **68**, 2164 (2023).
- [46] Z.-X. Chen, L.-L. Ma, S.-J. Ge, Z.-G. Chen, M.-H. Lu, Y.-F. Chen, and Y.-Q. Lu, Transient logic operations in acoustics through dynamic modulation, *Phys. Rev. Appl.* **21**, L011001 (2024).
- [47] Z.-X. Chen, Y.-G. Peng, Z.-G. Chen, Y. Liu, P. Chen, X.-F. Zhu, and Y.-Q. Lu, Robust temporal adiabatic passage with perfect frequency conversion between detuned acoustic cavities, *Nat. Commun.* **15**, 1478 (2024).
- [48] T. Laakso, V. Valimaki, M. Karjalainen, and U. Laine, Splitting the unit delay, *IEEE Sign. Proc. Mag.* **13**, 30 (1996).
- [49] J. O. Smith, *Physical Audio Signal Processing: For Virtual Musical Instruments and Audio Effects* (Stanford University, CCRMA, Stanford, CA, 2010),
- [50] L. Shao, W. Mao, S. Maity, N. Sinclair, Y. Hu, L. Yang, and M. Lončar, Non-reciprocal transmission of microwave acoustic waves in nonlinear parity-time symmetric resonators, *Nat. Electron.* **3**, 267 (2020).
- [51] T. Shah, C. Brendel, V. Peano, and F. Marquardt, Colloquium: Topologically protected transport in engineered mechanical systems, *Rev. Mod. Phys.* **96**, 021002 (2024).
- [52] C. Rasmussen, L. Quan, and A. Alù, Acoustic nonreciprocity, *J. Appl. Phys.* **129**, 210903 (2021).
- [53] Z. Li, K. Ding, and G. Ma, Eigenvalue knots and their isotopic equivalence in three-state non-Hermitian systems, *Phys. Rev. Res.* **5**, 023038 (2023).
- [54] J.-J. Liu, Z.-W. Li, Z.-G. Chen, W. Tang, A. Chen, B. Liang, G. Ma, and J.-C. Cheng, Experimental realization of Weyl exceptional rings in a synthetic three-dimensional non-Hermitian phononic crystal, *Phys. Rev. Lett.* **129**, 084301 (2022).
- [55] N. Hatano and D. R. Nelson, Localization transitions in non-Hermitian quantum mechanics, *Phys. Rev. Lett.* **77**, 570 (1996).
- [56] N. Hatano and D. R. Nelson, Vortex pinning and non-Hermitian quantum mechanics, *Phys. Rev. B* **56**, 8651 (1997).